

# Production and characterization of an AAV1-VP3-only capsid: An analytical benchmark standard

Mario Mietzsch,<sup>1,5</sup> Weijing Liu,<sup>2,5</sup> Ke Ma,<sup>3,5</sup> Antonette Bennett,<sup>1</sup> Austin R. Nelson,<sup>1</sup> Keely Gliwa,<sup>1</sup> Paul Chipman,<sup>1</sup> Xiaofeng Fu,<sup>4</sup> Shane Bechler,<sup>3</sup> Robert McKenna,<sup>1</sup> and Rosa Viner<sup>2</sup>

<sup>1</sup>Department of Biochemistry and Molecular Biology, College of Medicine, University of Florida, Gainesville, FL 32610, USA; <sup>2</sup>Thermo Fisher Scientific, 355 River Oaks Parkway, San Jose, CA 95134, USA; <sup>3</sup>Thermo Fisher Scientific, 490 Lakeside Dr., Sunnyvale, CA 94085, USA; <sup>4</sup>Biological Science Imaging Resource, Department of Biological Sciences, Florida State University, Tallahassee, FL, USA

**Adeno-associated viruses (AAVs) are non-enveloped ssDNA icosahedral T = 1 viruses used as vectors for clinical gene delivery. Currently, there are over 200 AAV-related clinical trials and six approved biologics on the market. As such new analytical methods are continually being developed to characterize and monitor the quality and purity of manufactured AAV vectors, these include ion-exchange chromatography and Direct Mass Technology. However, these methods require homogeneous analytical standards with a high molecular weight standard comparable to the mass of an AAV capsid. Described here is the design, production, purification, characterization, and the cryo-electron microscopy structure of an AAV1-VP3-only capsid that fulfills this need as a calibrant to determine capsid mass, charge, homogeneity, and transgene packaging characteristics.**

## INTRODUCTION

Recombinant adeno-associated viruses (rAAVs) are one of the most utilized vectors for the development and clinical application of gene delivery.<sup>1</sup> To date, six AAV vector-mediated gene therapies have gained approval as clinical biologics: Glybera, Luxturna, Zolgensma, Roctavian, Upstaza, and Hemgenix, either by the European Medicines Agency, the US Food and Drug Administration, or both.<sup>2-6</sup> Furthermore, over 200 clinical trials are ongoing and others awaiting approval for clinical use.<sup>7-9</sup> The AAV vectors are composed of a single-stranded DNA transgene expression cassette packaged into the T = 1 icosahedral protein capsid.<sup>10</sup> The capsids are ~26 nm in diameter and assembled from 60 viral proteins (VPs). The AAV expresses three overlapping VPs, VP1 (~80 kDa), VP2 (~65 kDa), and VP3 (~60 kDa), which are incorporated into the wild-type capsid at an approximate population ratio of 1:1:10.<sup>11,12</sup> The VPs share a common C terminus but vary in the length of their N termini. Compared with VP3, VP1 and VP2 are extended at their N termini with a shared ~65-amino-acid (aa) region and additional ~137 aa N-terminal to VP2 in the case of VP1.<sup>13</sup> The N-terminal regions of VP1 and VP2 contain conserved elements required for AAV infectivity such as a phospholipase A2 (PLA2) domain, a calcium-binding

domain, and nuclear localization signals, but they are not required for the capsid assembly.<sup>14,15</sup> Thus, capsids only composed of VP3 can be expressed and assembled.<sup>16</sup>

For AAV, 13 human and primate serotypes and numerous isolates have been described whose VP amino acid sequence identity varies between ~50% and 99%.<sup>17,18</sup> The capsid structures of all the AAV serotypes, as well as a select number of other natural isolates, and engineered variants have been determined by either X-ray crystallography and/or cryo-electron microscopy (cryo-EM).<sup>19,20</sup> In all AAV capsid structures determined, regardless of whether VP1 or VP2 are incorporated, structural ordering has only been observed for the VP3 region, with the exception of their N-terminal ~15 amino acids. The overall VP structure of the AAVs consists of a conserved  $\beta$  barrel core and variable surface topology formed from loops connecting the  $\beta$  strands.<sup>19</sup> The AAV capsids are assembled via icosahedral 2-, 3-, and 5-fold symmetry-related VP interactions and share similar morphologies, despite significant amino acid and structural differences of their surface loops.<sup>17</sup>

The AAV vectors are primarily produced in human embryonic kidney cells or in *Spodoptera frugiperda* insect cells.<sup>21,22</sup> Regardless of which cell system is used for manufacture, heterogeneities affecting the packaged genome and/or the capsid have been observed. A major by-product of all vector productions is empty AAV capsids, lacking the encapsidated vector genome.<sup>23</sup> Furthermore, various species of truncated genomes, variable ratios of incorporated VP1, VP2, and VP3 into the capsids, and different post-translational modifications (PTMs) have been described.<sup>11,12,24</sup> Thus, several quality control

Received 6 January 2023; accepted 4 May 2023;  
<https://doi.org/10.1016/j.omtm.2023.05.002>.

<sup>5</sup>These authors contributed equally

**Correspondence:** Robert McKenna, Department of Biochemistry and Molecular Biology, College of Medicine, University of Florida, Gainesville, FL 32610, USA.

**E-mail:** [rmckenna@ufl.edu](mailto:rmckenna@ufl.edu)

**Correspondence:** Rosa Viner, Thermo Fisher Scientific, 355 River Oaks Parkway, San Jose, CA 95134, USA.

**E-mail:** [rosa.viner@thermofisher.com](mailto:rosa.viner@thermofisher.com)

biophysical-based assays have been developed to characterize AAV vectors to ensure their purity before they are used in clinical trials, including analytical ultracentrifugation (AUC),<sup>25,26</sup> ion-exchange chromatography,<sup>27</sup> mass spectrometry (MS),<sup>28–35</sup> mass photometry,<sup>25,28,36,37</sup> cryo-EM,<sup>20,23</sup> and multi-angle light scattering (SEC-MALS).<sup>38</sup>

Ion-exchange chromatography can be either anion or cation exchange chromatography (AEX and CEX). AEX is commonly used for purification of AAV particles as the capsid typically has a negative charge.<sup>39,40</sup> Due to the presence of the negatively charged DNA inside the capsid, genome-containing (full) AAV capsids have a slightly lower isoelectric point (pI) than empty AAV capsids, enabling the separation and quantification of empty and full AAV particles.<sup>41</sup> Nonetheless, an AAV standard is required for chromatographic method development to verify the sufficiency of column equilibration as well as repeatability of retention time peak area.

In addition to AEX, native MS has become more common for the assessment of biomolecules under properly folded states.<sup>42,43</sup> However, the heterogeneous nature of AAV capsids poses the challenge of not being able to resolve the charge states of intact AAV particles by utilizing conventional native MS. To overcome this bottleneck, charge detection mass spectrometry (CDMS) has been developed for directly measuring the charge state of molecules,<sup>44–50</sup> proven to be invaluable for charge state unresolvable biomolecules such as AAV.<sup>28,32–35,51–54</sup> Compared with other common techniques for AAV characterization, CDMS is able to provide highly accurate and comprehensive molecular weight (MW) profiles, empty/full ratios, and charge state distributions in a single experiment within an hour.<sup>32,33,54,55</sup> Pierson et al. first reported AAV characterization using an electrostatic ion trap with a cylindrical charge detection tube.<sup>32</sup> Wörner et al. later demonstrated the capability of the Orbitrap analyzer for deriving charge states of AAV particles from the signal amplitude.<sup>52</sup> In parallel, Kafader et al. developed selective temporal overview of resonant ions (STORI) for charge state assignment of single-ion measurement on the Orbitrap platform.<sup>56</sup> It has been commercialized under the brand name “Direct Mass Technology mode” on a Q Exactive UHMR mass spectrometer. In order to assign the charge states of unknown samples via the STORI approach, a charge calibration curve established from known standards is required for Direct Mass Technology mode.<sup>57</sup> However, the prevalent protein standards of high MW, such as beta-galactosidase and GroEL from *E.coli*, are below 1 MDa and contain fewer than 100 charges. Therefore, a homogeneous resolvable AAV standard with charge states above 100 charges would be highly desirable for accurate charge assignment and calibration of megadalton species.

To fulfill the unmet need of having a homogeneous AAV capsid as an analytical standard, we developed an engineered adeno-associated virus serotype1 (AAV1) capsid variant containing only VP3 proteins. The capsid of AAV1 was chosen due to its lower rate of PTMs compared with other AAV serotypes.<sup>58</sup> In this study, the AAV1-VP3-only capsid is characterized by various biophysical methods to

demonstrate its homogeneousness. Thus, the engineered AAV1 capsid is a promising candidate as an analytical benchmark standard for the missing high-charge-state calibrant for Direct Mass Technology mode. Additionally, it can be used in multiple analytical techniques for system suitability tests in ion-exchange chromatography, MS, cryo-EM, or SEC-MALS analysis.

## RESULTS

### Generation of the AAV1 VP3 calibrant

The AAV serotype 1 was chosen for the generation of a homogeneous capsid sample AAV with the start codons for VP1 and VP2 removed (AAV1-VP3, Figure 1A). Following the purification of the sample, a single protein band migrating at ~60 kDa by SDS-PAGE was observed, consistent with the size of AAV1 VP3. Cryo-EM micrographs showed intact capsids of ~260 Å in diameter. The majority of AAV serotypes possess two potential ATG start codons for the expression of VP3 except for AAV7 and AAV9.<sup>30,59</sup> In AAV1, the first start codon initiates translation from methionine 203 (M203), resulting in VP3<sub>203-736</sub>, henceforth referred to as VP3<sub>M</sub>. The second start codon initiates translation from M211, resulting in an N-terminal truncated VP3 variant, VP3<sub>211-736</sub>, henceforth referred to as VP3<sub>m</sub> (Figure 1A). The later translation start leads to an eight amino acid (aa) shorter and ~0.7 kDa smaller protein, which is essentially impossible to differentiate by standard SDS-PAGE. Thus, a second sample was generated, in which the second ATG start codon was mutated to GTG, resulting in a methionine to valine amino acid substitution (M211V) of VP3 (AAV1-M211V-VP3, Figure 1B) and a mass change of ~32 Da. This change does not affect the *aap* gene situated in the alternative (+1) reading frame.<sup>16</sup> Consequently, this construct produced capsids comparable to the previous VP3-only plasmid, similarly showing a single protein band migrating at ~60 kDa by SDS-PAGE and intact capsids by cryo-EM analysis. To further ensure homogeneity of the standard, only empty capsids were produced. The cryo-EM micrographs confirmed that 99.74% (n = 1,537) and 99.87% (n = 25,205) of the capsids for the AAV1-VP3 and AAV1-M211V-VP3 samples were empty capsids.

### AAV1-VP3-only capsids are structurally identical to wtAAV1

Three-dimensional-image reconstruction of the empty AAV1-M211V-VP3 capsids, utilizing a total of 25,172 individual particles, resulted in a resolution of 2.27 Å, based on an FSC threshold of 0.143 (Table 1). The reconstructed capsid map displayed the characteristic surface features of the AAVs such as channels at the icosahedral 5-fold axes, three protrusions surrounding the 3-fold axes, and depressions at the 2-fold axes (Figure 2A). A cross-sectional view of the map showed the absence of electron density in the interior of the capsid since the sample was composed of empty capsids exclusively. The high resolution of the density map allowed the reliable building of an atomic model starting at the residue alanine 218 to the C-terminal leucine 736 with very well-ordered amino acid side chain densities (Figure 2B). Superposition of the refined model to the previously reported capsid structure of wild-type AAV1

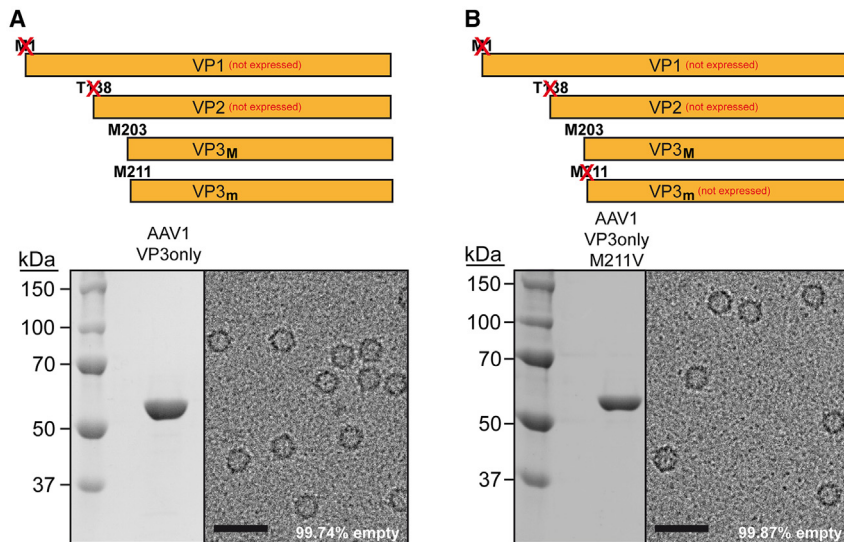


**Figure 1. Expression of AAV1-VP3-only capsid**

(A) Schematic depiction of the AAV1 cap ORF showing VP1, VP2, and VP3. The start codons for VP1 and VP2 are knocked out. Two possible start codons corresponding to methionine 203 and 211 express VP3. These two forms are labeled as VP3<sub>M</sub> (major) and VP3<sub>m</sub> (minor) and are not distinguishable in a standard SDS-PAGE. Example cryo-electron micrograph of AAV1-VP3-only capsids. The percentage of empty capsids in the sample is given. Scale bar: 50 nm. (B) Depiction as in (A) for AAV1-M211V-VP3-only capsid.

containing VP1, VP2, and VP3 (PDB: 3NG9), showed a C $\alpha$ -RMSD of 0.25 Å with no significant structural differences with the VP3 topology (Figure 2C). Thus, this structural characterization indicates that the AAV1 VP3 calibrant is structurally identical to the wild-type AAV1 capsid.

### Strong anion exchange chromatography

For this study a prototype strong anion exchange (SAX) column was used for the analysis of AAV particles. A SAX phase was chosen because the functional quaternary amine AEX groups are always cationic under all buffer conditions enabling adsorption and separation of AAV particles using both salt and pH gradients. In contrast, weak anion exchange phases may be less suitable as their re-equilibration time can be extensive as the stationary phase may buffer the mobile phase due to protonation or de-protonation of the 1°, 2°, or 3° amine groups near their pK<sub>a</sub>. The stationary phase of the SAX column is composed of 3- $\mu$ m nonporous, monodisperse particles. This particle size results in a bed with improved fluid mechanics for reduced analyte peak dispersion to provide higher resolution relative to polydisperse particles. A 2-mm-ID (internal diameter) column format was chosen to maximize the signal intensity by using low flow rates and to reduce the total amount of sample loading required for detection. A short 50-mm column was chosen to minimize the sample analysis time, which is made possible by the high-resolution power of the 3  $\mu$ m particles.

The fluorescence chromatograms of the AAV1-VP3 and AAV1-M211V-VP3 samples showed that the capsids are eluted at a salt concentration of ~230 mM tetramethylammonium chloride (23% MPB) and at a pH of ~5.0 (47% MPB) (Figures 3A and 3B). However, compared with AAV1-M211V-VP3, the AAV1-VP3 sample showed broader peaks in both the salt and pH gradient. Broad chromatographic peaks are an indication of multiple species in the sample and, thus, indicate a more heterogeneous sample. Comparatively,

the analysis based on UV chromatograms showed narrow bands in both salt and pH conditions and the absorbance at 280 nm was greater than at 260 nm, indicating that the sample contains viral protein and no nucleic acid (packaged genome) (Figures 3C–3F).

### RP-LC-MS analysis of dissociated capsid proteins

To further interrogate AAV1-VP3 and AAV1-M211V-VP3, the samples were characterized by MS. Both capsids were dissociated by acetic acid to release the individual VPs. The mass spectra of the dissociated VP3 proteins from AAV1-VP3 and AAV1-M211V-VP3 are shown in Figure 4A. Both constructs showed charge envelopes ranging from m/z 900 to 2,200. In addition to the main envelope, some minor forms were observed at the bottom of the spectra (Figure 4A). The deconvolution results shown in Figure 4B exhibited that the most abundant form of AAV1-VP3 was detected at 59,516.02 Da. This correlates well with the theoretical MW of VP3<sub>M</sub> after methionine (M203) removal and acetylation of A204 at the N termini. The minor form at 58,887.336 Da corresponds to the sequence with the N-terminal truncated VP3<sub>m</sub> form starting with an acetylated alanine (A212). All the identified proteoforms corresponded to previously described AAV1 VP3 proteins.<sup>60</sup> The N-terminal methionine excision and N-terminal acetylation (NTA) are two of the most common protein post-translational modifications in eukaryotes.<sup>61,62</sup> No additional PTMs, such as ubiquitination, phosphorylation, SUMOylation or glycosylation, were observed in this analysis as expected.<sup>58</sup> The ratio between the minor and major VP3 forms is approximately 1:13 (or 8% VP3<sub>M</sub>). The VP3<sub>m</sub> form is expressed when translation at the first ATG start codon is not initiated and instead the second ATG is utilized (Figure 1A). This second ATG is conserved in the majority of AAV serotypes with the exception of AAV9.<sup>30,59</sup> The reason for the conservation is unclear as capsid production is unaffected if the first start codon is mutated (data not shown), which resembles AAV7 that only possesses the second start codon.<sup>63</sup> For the AAV1-M211V-VP3 construct, the second ATG is mutated (Figure 1B). Consequently, the N-terminal truncated form starting at A212 was not detected, confirming that the second ATG start codon contributed to the heterogeneity. The measured MW of AAV1-M211V-VP3 at 59,483.86 Da is within 16 ppm mass accuracy compared with its theoretical MW modified with NTA. Both AAV1-VP3 and AAV1-M211V-VP3

**Table 1. Summary of cryo-EM data collection and refinement statistics**

Cryo-EM data and refinement parameter	AAV1-M211V-VP3 only
Total number of micrographs	4,418
Defocus range ( $\mu\text{m}$ )	0.49–1.70
Electron dose ( $e^{-}/\text{\AA}^2$ )	59
Frames/micrograph	102
Pixel size ( $\text{\AA}/\text{pixel}$ )	0.94
Capsids used for final map	25,172
Resolution of final map ( $\text{\AA}$ )	2.27
PHENIX model refinement statistics	
Residue range	218–736
Map CC	0.900
RMSD bonds ( $\text{\AA}$ )	0.01
RMSD angles ( $^{\circ}$ )	0.88
All-atom clash score	8.30
Ramachandran plot	
Favored (%)	97.9
Allowed (%)	2.1
Outliers (%)	0
Rotamer outliers (%)	0
C- $\beta$ deviations	0

samples contained several other very minor N-terminal and C-terminal fragments of VP3, due to protein backbone clipping starting at N terminus of proline 210 (P210), 1:15 ( $\sim 7\%$ ) relative to VP3<sub>M</sub>, or C terminus of aspartate 556 (D556), 1:100 ( $\sim 1\%$ ) relative to VP3<sub>M</sub>. The cleavage after D556 is not observed in the cryo-EM map due to its low abundance. All sequence variants of AAV1-VP3 and AAV1-M211V-VP3 were further confirmed by top-down analyses shown in Figure S1 and/or by accurate mass measurements. Hence, MS results of dissociated VP3 proteins not only demonstrated that the main species in AAV1-VP3 and AAV1-M211V-VP3 match up with target MW, but they also corroborate the improvement in homogeneity resulting from the open reading frame (ORF) start modification.

#### Intact capsid analyses by ensemble native MS measurement

After determining the sample homogeneity integrity under denatured condition, ensemble native MS was utilized to investigate the assembly of intact virus particles. Native mass spectra of AAV1-WT, AAV1-VP3, and AAV1-M211V-VP3 shown in Figure 5A display charge envelopes above  $m/z$  20,000. AAV1-WT is present at relatively higher  $m/z$  and gives the broadest peak distribution compared with AAV1-VP3 and AAV1-M211V-VP3. Furthermore, its charge states are unresolvable by ensemble measurement due to sample complexity. Consequently, the AAV1-WT spectrum is too heterogeneous, and any attempts of deconvolution yielded random unreliable peaks ranging from 3 to 4 MDa. On the contrary, the charge states of both AAV1-VP3 and AAV1-M211V-VP3 are resolvable with the center charge state at 168+. Although both AAV1-VP3 and AAV1-M211V-VP3 reveal a main charge envelope deconvoluted to be

3.57 MDa as the most abundant component, there is at least a second minor charge envelope existing at slightly higher  $m/z$  relative to the main charge envelope. The relative abundance of the second envelope in AAV1-M211V-VP3 ( $\sim 15\%$ ) was significantly lower than the one for AAV1-VP3 ( $\sim 40\%$ ). The difference in relative abundance reflects better uniformity of AAV1-M211V-VP3, which is also confirmed by the deconvoluted MW profile (Figure 5B). More peaks were observed in the deconvoluted spectrum of AAV1-VP3 compared with AAV1-M211V-VP3 spectrum. Calculation of measured MW of dissociated VP3 proteins from AAV1-VP3 (Figure 4B) containing forms starting at A204, P210, or A212 gives intact particle MWs at 3.572 MDa, 3.544 MDa, and 3.533 MDa, respectively. The most abundant peak from native MS deconvoluted at 3.57 MDa demonstrates the correct assembly of 60 VP3 proteins starting at A204. The second and third abundant peaks at 3.549 MDa and 3.534 MDa exhibit some heterogeneity due to presence of truncated/clipped proteoforms. This indicates the mixed assembly of VP3 proteins starting at A204, P210, and A212. Some higher MW forms above 3.57 MDa are possibly due to non-covalently surface bound process-related impurities or remaining solvent adducts. Compared with AAV1-VP3, the deconvoluted spectrum of AAV1-M211V-VP3 showed one dominant peak at 3.57 MDa. This is close to the calculated mass of AAV1-M211V-VP3 at 3.569 MDa, less than 0.05% from the theoretical value. Analyses of both denatured VP3 proteins and native intact virus particles confirmed that the mutation of the second ATG start codon enhanced the sample homogeneity.

#### Single-ion measurement of intact capsid via Direct Mass

##### Technology mode

Due to its ultra-high MW and ultra-high charge states, as well as its remarkable homogeneity, AAV1-M211V-VP3 is a promising candidate as a charge calibrant for Direct Mass Technology mode to fill the need for a high-charge-state calibrant. To evaluate the samples, the calibration coefficient profiles from AAV1-VP3, AAV1-M211V-VP3, and AAV1-WT were compared (Figures 6A–6C). As aforementioned, Kafader et al. developed STORI approach for tracking individual ion signals in an Orbitrap mass analyzer.<sup>56,57</sup> The charge state of a single ion and the slope of its STORI plot are in a linear relationship with a slope K (charge = STORI slope/K). This K is the calibration coefficient that has 10% variation across different instruments. The calibration algorithm generates a set of mass spectra from all single ions using a range of K values and their corresponding  $m/z$  and charge states pairs. The algorithm calculates the simplicity score, or self-dot product, for each constructed mass spectrum. The optimal calibration coefficient is the K that generates the simplest spectrum with the lowest simplicity score. This “seeking simplest spectrum” approach necessitates homogeneity of the calibrant. While the AAV1-WT sample generated a noisy profile leading to an ambiguous calibration coefficient (Figure 6C), the AAV1-M211V-VP3 sample constructed a Gaussian curve yielding a calibration coefficient at 47,286 (Figure 6B). Although, the AAV1-VP3 sample also resulted in a similar calibration coefficient at 47,383, its profile shape is not as symmetric as AAV1-M211V-VP3, indicating more heterogeneity (Figure 6A). Thus, AAV1-M211V-VP3 is the

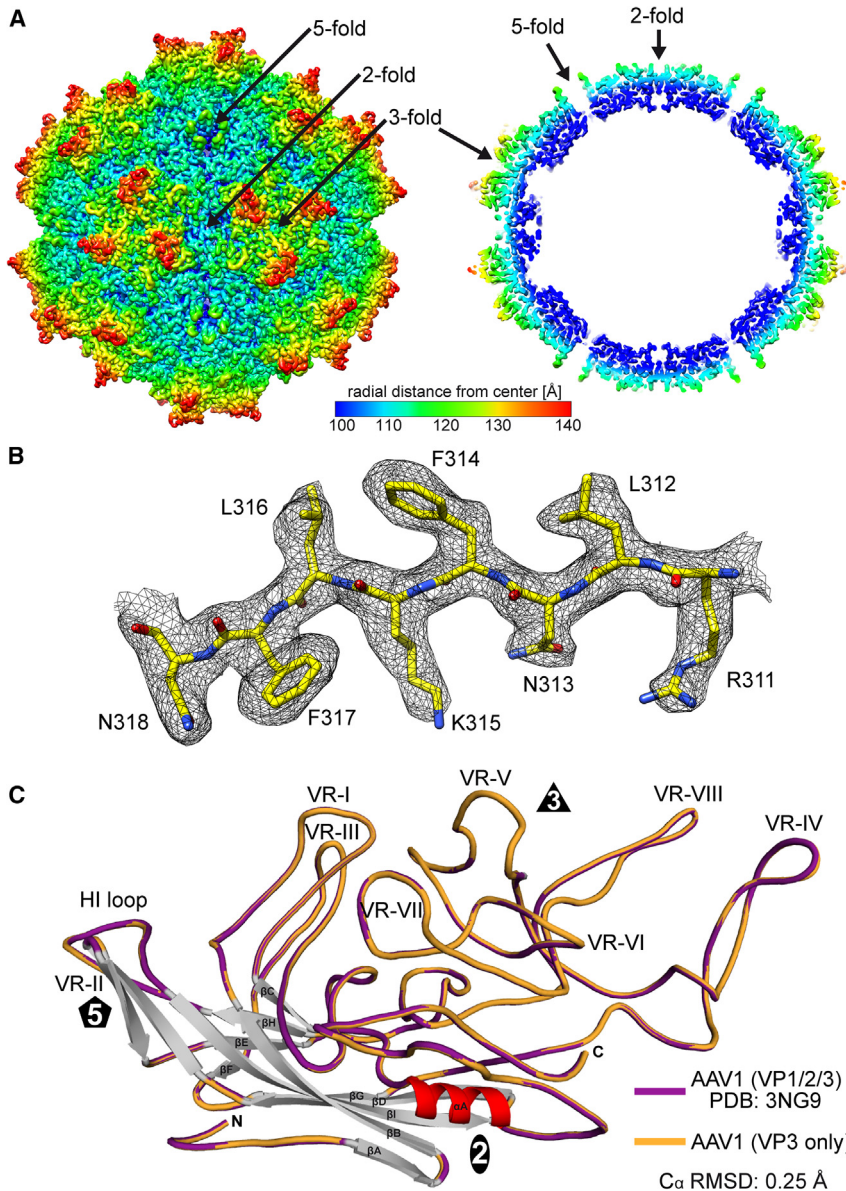


**Figure 2. Capsid structure of AAV1-M211V-VP3-only capsid**

(A) The capsid surface (left) and cross-sectional (right) density map determined by cryo-EM reconstruction are shown. The reconstructed maps are radially colored (blue to red) according to distance to the particle center, as indicated by the scale bar. The icosahedral 2-, 3-, and 5-fold axes are indicated. (B) Amino acid residues modeled for the  $\beta$ D strand are shown inside their density maps (in black). The amino acid residues are labeled and shown as stick representation and colored according to atom type: C = yellow, O = red, N = blue. (C) Superposition of AAV1-VP1/2/3, PDB: 3NG9 (purple), and AAV1-M211V-VP3-only (orange). The  $\beta$  barrel core motif ( $\beta\beta$ - $\beta$ l),  $\beta$ A, and the  $\alpha$ A helix are indicated. The VRs (VR-I to VR-IX) and the N and C termini are labeled, and the approximate icosahedral 2-, 3-, and 5-fold axes are represented by an oval, triangle, and pentagon, respectively.

obtained predicted MWs of empty AAV1-WT capsids (Figure 7B) at 3.77 MDa and a commercially available empty AAV8 sample at 3.73 MDa (Figures 7C, and S2) with small subpopulation of heavier particles and on average broader peaks probably due to post-translational processing.<sup>58</sup> Utilizing the calibration curve for the Direct Mass Technology mode, the analysis of another commercially available AAV8 sample containing a CMV-GFP transgene cassette showed a mixture of empty (0.8%), partial (8.6%), and full capsids (73.1%), as well as capsids with oversized genomes (17.4%) (Figure 7D). The significant amount of capsids with oversized genomes is likely caused by the small size of the vector genome cassette of  $\sim$ 2.55 kb allowing continuous packaging of dimer replication forms. Mass domain spectra showed the MW of empty capsids at  $\sim$ 3.70 MDa, and full capsids center around  $\sim$ 4.36–4.46 MDa, matching the expected MW.<sup>28</sup> In summary, AAV1-M211V-VP3 extends the valid charge states range of a calibration curve

best calibrant candidate among these three AAV samples. Moreover, AAV1-M211V-VP3 showed a clean individual ion spectrum that follows the principle of CDMS, charge state in proportion to signal intensity (Figure 6D). Including the AAV1-M211V-VP3 sample along other calibrants (Figures 6D–6H) showed individual ion spectra from all calibrants covering a wide range of MW (29–3.57 MDa) and charge states (9+ to 173+) and established a calibration curve that provided a unique calibration coefficient, 47,052 in this case, for a particular mass spectrometer (Figure 6I).

To validate the calibration curve by applying it for AAV1-M211V-VP3 MW calculation, the measured MW of the sample expectedly equaled the theoretical MW of 3.57 MDa (Figure 7A). Similarly, we

for Direct Mass Technology mode to over 170 charges. The calibration curve has been successfully employed for measuring heterogeneous AAV samples to reveal MW profile and ratio of empty/full capsids.

## DISCUSSION

Current available protein standards for various applications usually do not exceed 1 MDa. Thus, when samples such as AAV vectors, with a mass of  $>$ 3.5 MDa, are analyzed, they are usually well outside the range of the standard series. Thus, we have developed an engineered AAV1 capsid as an analytical standard. AAV1 was chosen due to its lower rate of PTMs compared with other AAV serotypes,<sup>58</sup> a beneficial characteristic for an analytical standard. To ensure the

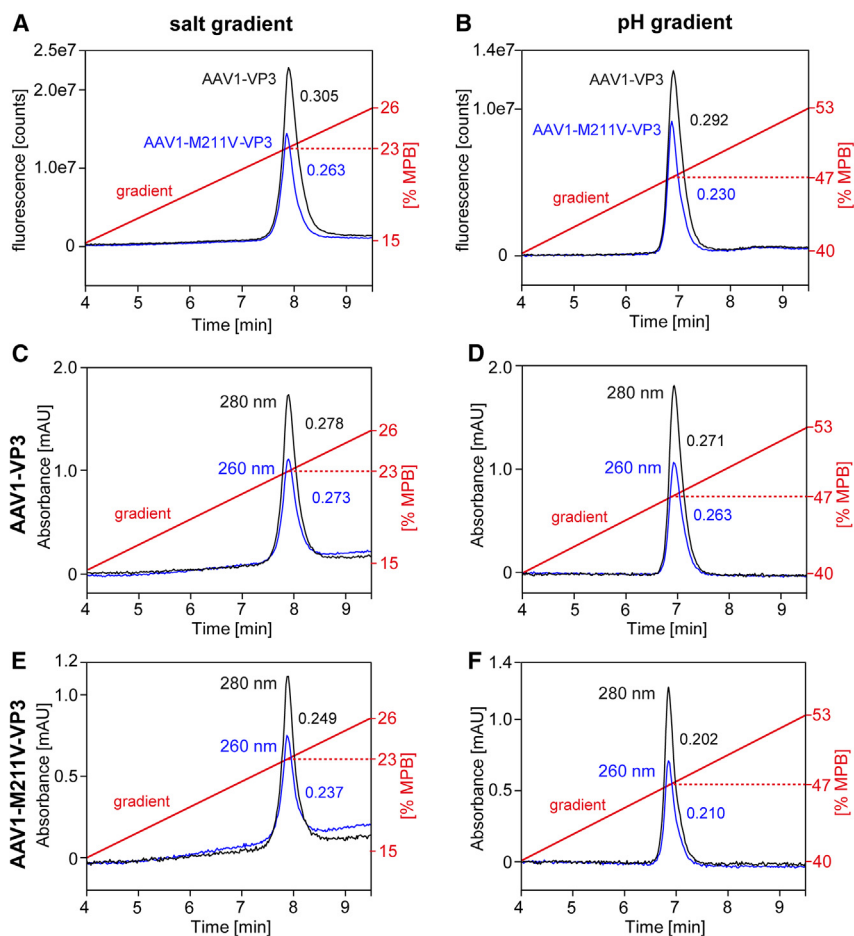


**Figure 3. Characterization of AAV1-VP3-only capsids by strong anion exchange liquid chromatography**

(A) Fluorescence chromatograms of intact AAV1-VP3 and AAV1-M211V-VP3 using a salt gradient. (B) Fluorescence trace of AAV1-VP3 and AAV1-M211V-VP3 samples from a pH gradient. (C and D) UV chromatograms of intact AAV1-VP3 (E and F) and AAV1-M211V-VP3 from salt and pH gradient respectively. The peak width at half height is given in each panel.

applications.<sup>41</sup> Additionally, the AAV1 VP3 standard has the potential as an excellent candidate for both the column's quality control and early-stage method development purposes.

The homogeneity of the assembled capsids was further demonstrated by MS, with AAV1-M211V-VP3 outperforming AAV1-VP3. For the AAV1-M211V-VP3 sample, ensemble native MS detected less than 15% of minor species, and its calibration coefficient for constructing charge calibration curve is within 0.5% relative standard deviation from other calibrants. The consistent calibration coefficient observed for AAV1-M211V-VP3 indicates that the Orbitrap mass analyzer exhibits a linear response for single ions, even at ultra-high charge states. AAV1-M211V-VP3, as a high-charge-state calibrant, extends an accurate charge-based calibration curve over 170 charges and therefore increases intrinsic mass accuracy for species above 1 MDa. Without

highest possible uniformity, only empty capsids were produced, and the second start codon for VP3 was eliminated (M211V). Despite these changes, structural characterization via cryo-EM indicates that the AAV1-VP3 sample is structurally identical to the wild-type AAV1 capsid (Figure 2). This is not surprising as previous studies have not shown any significant structural differences between empty and full capsids.<sup>64,65</sup> Furthermore, the “rod-like” density inside the 5-fold channel that was previously observed in empty and full AAV capsids is also present in the AAV1-VP3 only cryo-EM map (data not shown). In the absence of VP1, VP2, or a packaged genome, this density can therefore only be attributed to the N terminus of VP3. Previously, we suggested that due to the narrow diameter of the channel, a stretch of amino acids with small side chains is likely present,<sup>64–66</sup> which is also the case for the AAV1 VP3 N terminus (aa204 to 212: ASGGGAPVA).

The SAX chromatography showed that the AAV1-M211V-VP3 sample is predominantly empty, which confirmed the cryo-EM data with >99% empty capsids. Furthermore, homogeneous overall charge for the viral capsids at each pH was observed. These properties make this sample an ideal standard to calibrate the SAX columns utilized to determine the empty-to-full ratio of samples used for gene therapy

having AAV1-M211V-VP3 as the high-end charge state calibrant, we are relying on extrapolating the calibration curve established with highest charge state  $\sim 70$ , given by GroEL. The consequence of using calibration extrapolation is that it may introduce errors and reduce the accuracy of measurements. Accurate mass and particle ratios measurement for AAV1 and AAV8 samples were achieved (Figure 7) by incorporating AAV1-M211V-VP3 into the calibration. This demonstrates that Direct Mass Technology mode is an excellent tool for evaluating post-production composition of AAV as well as its DNA packaging, similar to other CDMS approaches.<sup>28,33</sup> Direct Mass Technology mode can resolve and accurately quantify the variable partially filled particles, setting it apart from assays that usually only distinguish between empty or filled capsids (ion chromatography, dynamic light scattering, etc.).

Therefore, AAV1-M211V-VP3 not only fulfills the need of having high-charge-state calibrant for Direct Mass Technology mode/CDMS, but it also can be used for system suitability tests in ion-exchange chromatography, MS, mass photometry, cryo-EM, or SEC-MALS analyses. This AAV1-M211V-VP3-only capsid is a promising candidate as an analytical benchmark standard or calibrant for multiple analytical techniques, including CDMS, which provides

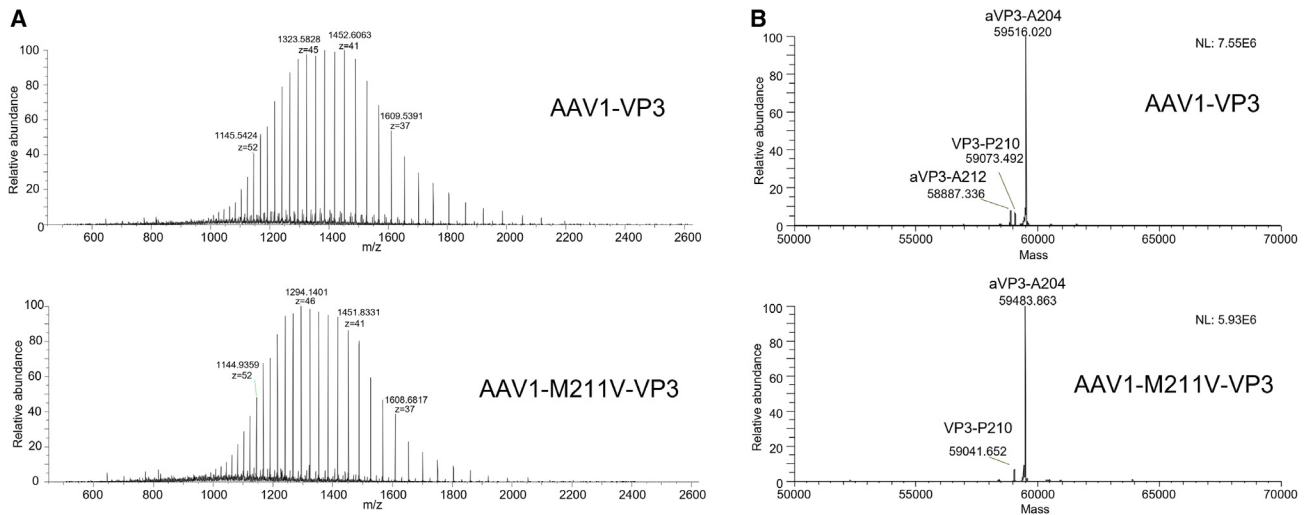


**Figure 4. Mass spectrometry analysis of AAV1 capsids under denaturing conditions**

(A) RP-LC-MS and (B) deconvoluted spectra of AAV1-VP3 and AAV1-M211V-VP3. Each peak is labeled with the corresponding sequence variant. For example, aVP3-A204 indicates N termini starting at Ala204 with acetylation.

a time-efficient, accurate, and comprehensive MW profile, empty/full ratio, and charge state distribution in a single experiment and will likely play a critical role in AAV characterization in the foreseeable future.

## MATERIALS AND METHODS

### Cell culture

HEK293 cells were maintained adherent in Dulbecco's Modified Eagle Medium (Thermo Fisher, Waltham, MA), supplemented with 10% heat-inactivated fetal calf serum and 100 units of penicillin/ml and 100  $\mu$ g of streptomycin (Caisson Laboratories, Smithfield, UT) at 37°C in 5% CO<sub>2</sub>.

### Site-directed mutagenesis

The AAV1-VP3only plasmid, described previously,<sup>12</sup> containing AAV2 *rep* and AAV1 *cap* with a mutated VP1 and VP2 start codon served as the template for site-directed mutagenesis PCR. For the generation of the AAV1-VP3only M211V plasmid, PCR primers were designed that contained the desired mutation, which was flanked on both sides by 17 or 18 homologous nucleotides. Primers were ordered from Sigma-Aldrich (Houston, TX) and used in PCR amplification reactions using a C1000 Touch thermal cycler (Bio-Rad, Hercules, CA) and *Pfu* Turbo DNA polymerase AD (Agilent, Santa Clara, CA). PCR products were incubated at 37°C overnight with *DpnI* restriction enzyme (NEB, Ipswich, MA) to degrade the methylated template plasmid. The reactions were then transformed into DH5 $\alpha$  competent cells (NEB, Ipswich, MA), which were cultured on LB-ampicillin selective media and further amplified to isolate the plasmid. Clones were submitted for Sanger sequencing (Genewiz-Azenta, South Plainfield, NJ) to verify the introduced mutation.

### Recombinant AAV production and purification

AAV1 VP3-only capsids were produced by double transfection of HEK293 cells, utilizing pHelper (Stratagene) and the AAV1-VP3-only plasmid (or the M211V variant). In absence of the plasmid containing an ITR-flanked genome, primarily empty capsids will be generated. The transfected cells were harvested 72 h post transfection, washed with phosphate-buffered saline (PBS; 137 mM NaCl, 2.7 mM KCl, 100 mM Na<sub>2</sub>HPO<sub>4</sub>, 2 mM KH<sub>2</sub>PO<sub>4</sub>), and the cells pelleted and resuspended in PBS with 1 mM MgCl<sub>2</sub> and 2.5 mM KCl. The resuspended cells were subjected to three freeze-thaw cycles (−80°C–37°C) and subsequently incubated with 125 units/mL benzonase for 1 h at 37°C before centrifugation at 10,000  $\times$  g for 15 min to pellet the cell debris. The supernatants were purified by iodixanol gradient ultracentrifugation as previously described.<sup>67</sup> The 25% fraction of the gradient was subsequently purified by AVB Sepharose affinity chromatography and concentrated as previously described.<sup>68</sup> The sample was analyzed by SDS-PAGE to confirm its purity and the concentration by comparing it to BSA standards. Utilizing the MW of the capsid, the protein concentration was converted into capsids/ml. The empty AAV8 and AAV8-CMP-GFP sample produced in insect Sf9 cells were purchased from Virovek (Hayward, CA), Lot#19-564E and Lot#20-457 (Figure S2).

### Cryo-EM data collection

The purified AAV1-M211V-VP3-only capsids were loaded onto a glow discharged holey carbon-coated grid (Protochips) and incubated at 4°C at 95% humidity for 3.0 s within the Vitrobot Mark IV (Thermo Fisher Scientific, Waltham, MA, USA). Following this, excess sample was blotted by the machine and the grids vitrified by plunging into liquid ethane. The vitrified grids were analyzed for their ice thickness and sample distribution using a 200-kV FEI Tecnai G2 F20-TWIN transmission electron microscope (FEI, Hillsboro,

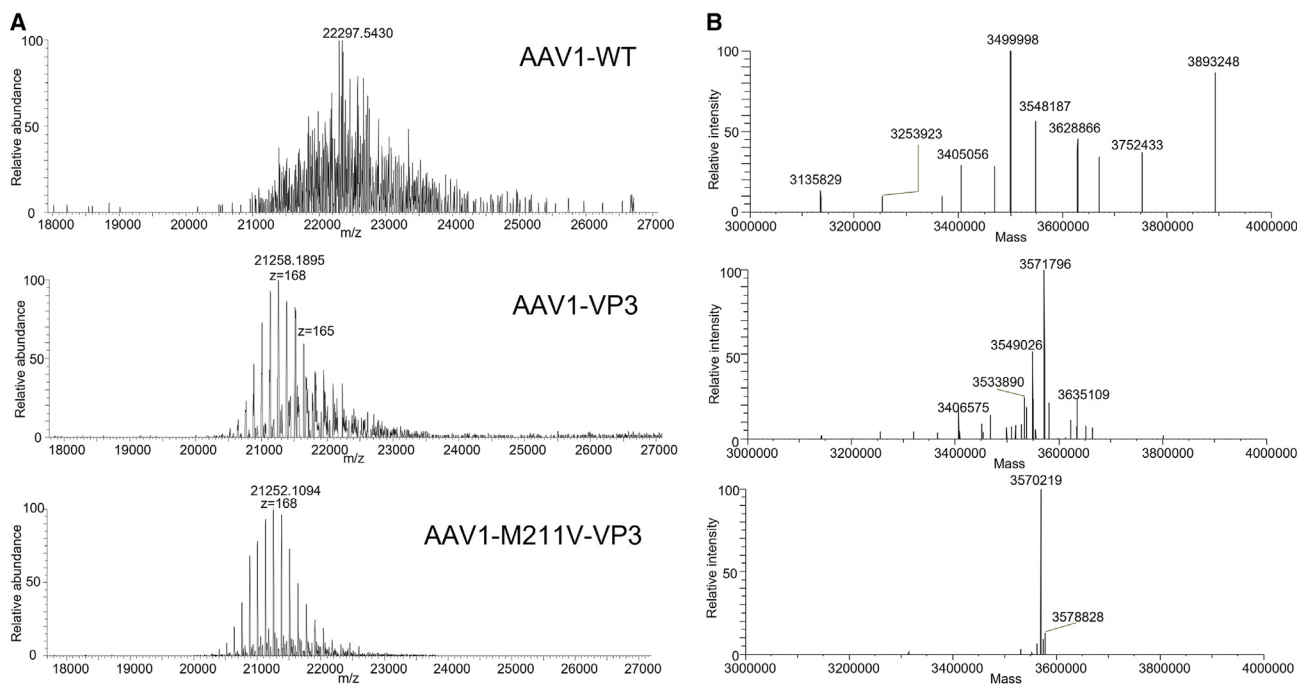


**Figure 5. Native mass spectrometry analysis of AAV1 capsids**

(A) Ensemble native MS spectra and (B) deconvoluted spectra of intact AAV1-VP3, AAV1-M211V-VP3, and AAV1-WT (containing VP1, VP2, and VP3) particles using 25K @m/z 400 resolution (128 msec transient).

Oregon, USA) at  $\sim 20 \text{ e}^-/\text{\AA}^2$ . High-resolution data collections were conducted at the Biological Science Imaging Resource at the Florida State University. Data were collected on a Titan Krios electron microscope operating at 300 kV and equipped with a DE-Apollo direct electron detector (Direct Electron, San Diego, CA, USA). A total of 102 movie frames were collected per micrograph at an electron dose of  $\sim 59 \text{ e}^-/\text{\AA}^2$ . The raw movie frames were aligned utilizing MotionCor2 with dose weighting, to generate the motion-corrected micrographs.<sup>69</sup>

### 3D image reconstruction

For the 3D image reconstruction of AAV1-VP3-only capsids, the motion-corrected micrographs were imported into the cisTEM software package.<sup>70</sup> Micrographs of poor quality were identified using the CTF estimation subroutine and excluded for the reconstruction. Particles were picked automatically and subjected to 2D classification. 2D classes containing clear viral capsid features were selected and used for the generation of an *ab initio* model by 3D reconstruction. This *ab initio* model was further refined using the default settings, and the final density map was sharpened with a pre-cutoff B-factor value of  $-90 \text{ \AA}^2$  and post-cutoff B-factor value of  $50 \text{ \AA}^2$ . The resolution of the reconstructed density map was estimated based on Fourier shell correlation of 0.143.

### Model building

The existing model of AAV1 capsid (PDB: 3NG9) was docked into the EM density map by using the “fit in map” feature within UCSF

Chimera.<sup>71</sup> The fit of the 60 mer with respect to the EM density map was then improved by adjusting the voxel size that maximizes the correlation coefficient. The voxel size-adjusted EM density map was then imported into Coot where manual model building and real space refine tools were used to adjust the AAV1 VP3 model where necessary.<sup>72</sup> The 60 mer of the AAV1 VP3 model was automatically refined using the real space refine subroutine in PHENIX, which also provided the refinement statistics.<sup>73</sup>

### Anion exchange chromatography

The AEX separation of AAV samples was performed using a ProPac 3R SAX 3  $\mu\text{m}$  HPLC column (3- $\mu\text{m}$  monodisperse particles, 2 mm  $\times$  50 mm) (Thermo Fisher Scientific, Sunnyvale, CA, USA) on a Thermo Scientific Vanquish Flex UHPLC system (Thermo Fisher Scientific, Germering, Germany) equipped with a Vanquish quaternary pump, a Vanquish Variable Wavelength Detector, and a Vanquish Fluorescence Detector (FLD).

For salt gradient method separations, mobile phase A (MPA) was Milli-Q water, mobile phase B (MPB) contained 1 M tetramethylammonium chloride (MilliporeSigma, St. Louis, MO) in Milli-Q water, and mobile phase C (MPC) contained 200 mM bis-tris propane (MilliporeSigma, St. Louis, MO) in Milli-Q water. MPC was adjusted to pH 9.5 using 5 M hydrochloric acid. The flow rate was 0.2 mL/min. The gradient consisted of 15%–35% MPB from 0 to 10 min, 35%–90% MPB from 10 to 10.1 min, and 90% MPB until 12 min. MPB was reduced to 15% from 12 to 12.1 min and then maintained

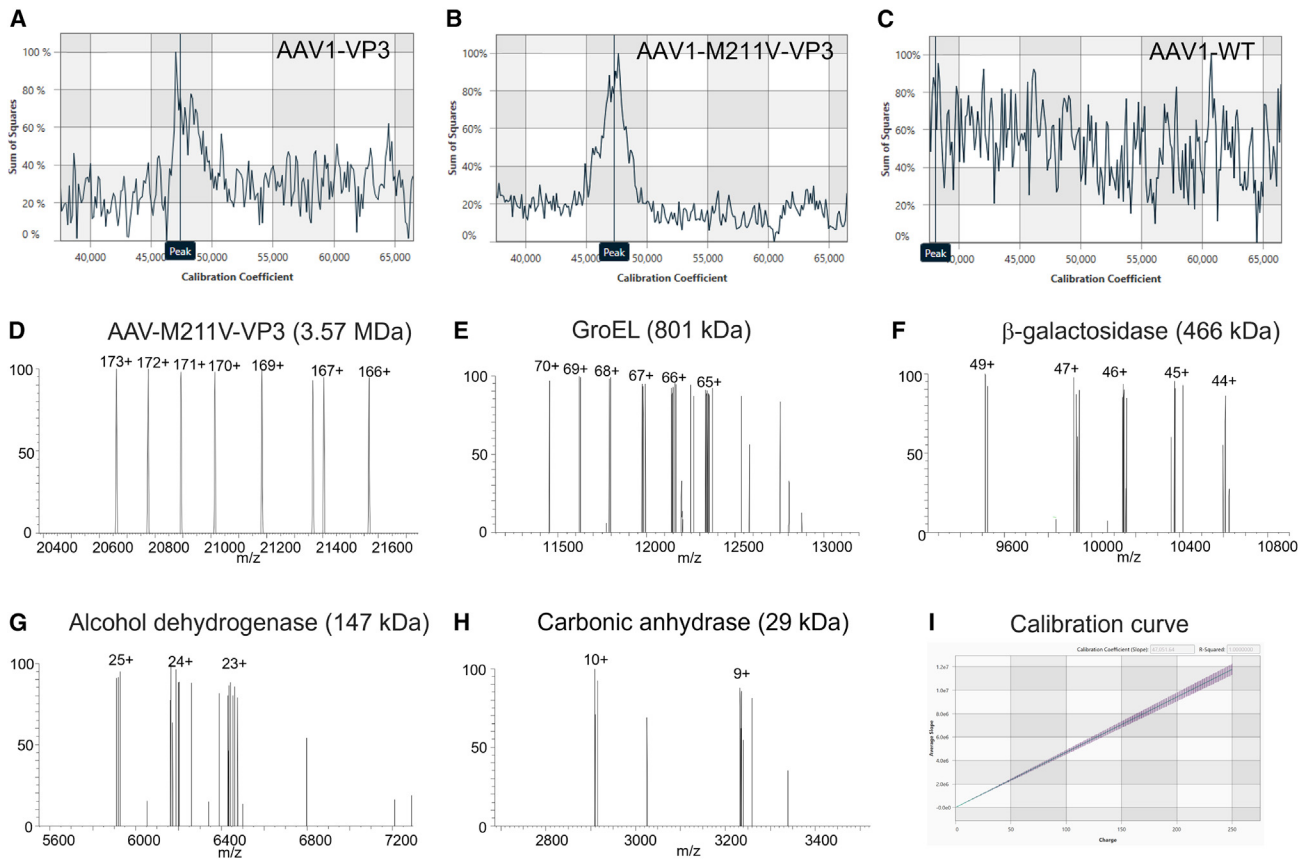


**Figure 6. Calibration for Direct Mass Technology mode analysis**

Calibration coefficient profiles of (A) AAV1-VP3, (B) AAV1-M211V-VP3, and (C) AAV1-WT. (D–H) Individual ion spectra of calibrants for Direct Mass Technology mode and (I) established linear calibration curve out of the five calibrants. The calibration coefficient is 47,052.

at 10% until the end of the 19-min gradient. The gradient contained 10% MPC throughout the whole gradient. The column temperature was set at 30°C. Prior to the experiment, the AAV1-VP3 capsids (~0.5 mg/mL) were diluted 10 times with Milli-Q water. 2  $\mu$ L of the sample (100 ng or  $1.5 \times 10^{10}$  capsids) was injected for UV detection at 260 and 280 nm. For fluorescence detection, 0.1  $\mu$ L (5 ng or  $7.5 \times 10^8$  capsids) was injected with excitation and emission wavelengths of 280 and 330 nm, respectively.

For pH gradient method separation, MPA contained 20 mM ammonium bicarbonate and 15 mM ammonium hydroxide in Milli-Q water, and MPB contained 30 mM acetic acid and 15 mM formic acid in Milli-Q water. No pH adjustment was needed. The flow rate was 0.2 mL/min. The gradient consisted of 40% MPB from 0 to 0.5 min, 40%–80% MPB from 0.5 to 15.5 min, 80%–100% MPB from 15.5 to 15.6 min, and 100% MPB until 18 min. MPB was reduced to 40% from 18 to 18.1 min and then maintained at 40% until the end of the 30-min gradient. The column temperature was set at 30°C. Similar as above, 2  $\mu$ L of the sample (100 ng or  $1.5 \times 10^{10}$  capsids) was injected for UV detection at 260 and 280 nm, and 0.1  $\mu$ L (5 ng or  $7.5 \times 10^8$  capsids) of the sample was injected for fluorescence detec-

tion with excitation and emission wavelengths of 280 and 330 nm, respectively. The Thermo Scientific Chromeleon 7.2.10 Chromatography Data System was used for instrument control and analysis of the chromatographic data.

#### Mass spectrometry

MS analyses of the AAV1 VP3 samples (10  $\mu$ g or  $1.5 \times 10^{12}$  capsids per experiment) included dissociated VP3 proteins analysis by reverse phase-liquid chromatography-mass spectrometry (RP-LC-MS), intact capsid analyses by ensemble native MS measurement, and single-ion measurement via Direct Mass Technology mode. To dissociate VP3 proteins from AAV capsid, samples were buffer exchanged and concentrated into 200 mM ammonium acetate using Amicon Ultra-0.5 Centrifugal Filter (100 kDa molecular weight cutoff [MWCO]). The collected sample was added with 10% acetic acid and incubated at room temperature for 30 min.<sup>30</sup> RP-LC-MS analyses were performed on Thermo Scientific Vanquish Neo Ultra-High-Performance Liquid Chromatography system coupled to Thermo Scientific Q Exactive UHMR mass spectrometer. The separation was performed on a Thermo Scientific EASY-Spray Accucore C4 column (150 mm  $\times$  150 mm) at a flow rate of 0.8 mL/min with column

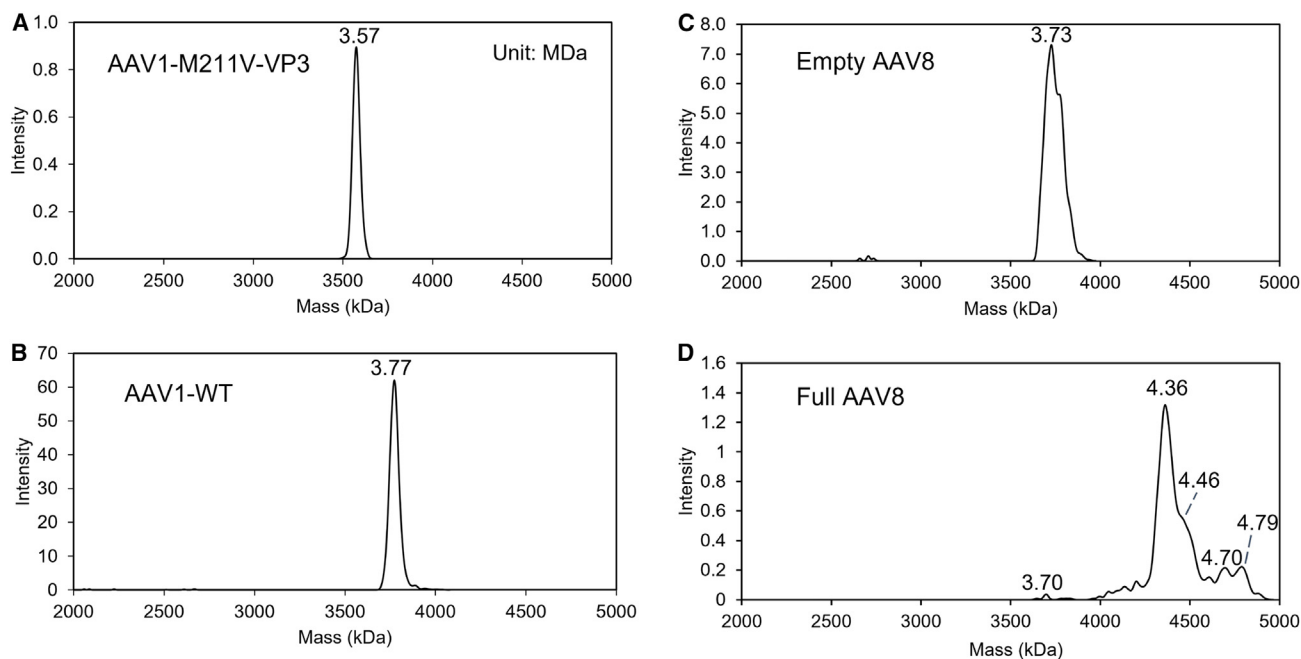


**Figure 7. Utilization of Direct Mass Technology**

Direct Mass Technology mode analysis of (A) AAV1-M211V-VP3, (B) AAV1-WT (containing VP1, VP2, and VP3), and (C) empty and (D) full AAV8 capsids.

temperature at 60°C. The proteins were eluted using a linear gradient from 20% to 80% B (0.1% formic acid in acetonitrile) over 15 min. The source parameters for Q Exactive UHMR were as follows: source voltage 2.3 kV; capillary temperature 320°C; S-lens RF level: 100%, trapping gas pressure readout at  $\sim 2 \times 10^{-11}$  mbar. Data were acquired under intact protein mode with 5 mscan at 12.5K @m/z 400 resolution. Top-down analyses were performed using all ion fragmentation by setting collision energy at 20 eV and using 5 mscan at 100K @m/z 400 resolution.

Ensemble native MS measurement and Direct Mass Technology mode analyses were performed on Thermo Scientific Q Exactive UHMR. Prior to native and Direct Mass Technology mode MS analysis, samples were buffer exchanged into 200 mM ammonium acetate using Amicon Ultra-0.5 Centrifugal Filter (100 kDa MWCO,  $10,000 \times g$  for 5 min, 4°C) and repeated six times. The sample was loaded into Au/Pd-coated borosilicate emitters (Thermo Scientific, ES388) for nano-ESI. For instrument parameters, ion transfer target m/z and detector optimization were set to “high m/z.” In-source trapping was set at  $-50$  V, and extended trapping voltage was set from 0 to 100 eV. Trapping gas pressure readout was in the range of  $3 \times 10^{-10}$  to  $6 \times 10^{-10}$  mbar. Data were acquired at 6–25K @m/z 400 resolution settings with transient averaging enabled. For Direct Mass Technology mode acquisitions, most of the tuning parameters were kept as for ensemble native MS. However, sample dilution, reduction of trapping gas pressure, and injection time were optimized for achieving single-ion scan. Exemplary readout of trapping gas pressure is  $2 \times 10^{-10}$  mbar for AAV. The Direct Mass Technology data-

sets were acquired using 50–100K@m/z 400 resolution for 15–60 min. The RP-LC-MS and ensemble native MS data were processed by Thermo Scientific BioPharma Finder 5.0 software. Data acquired by Direct Mass Technology mode were processed by STORIBoard software (Proteinaceous, Chicago IL).

#### DATA AVAILABILITY

The AAV1-M211V-VP3 cryo-EM reconstructed density map and model built for the capsid were deposited in the Electron Microscopy DataBank with the accession numbers EMD: 29377 and PDB: 8FQ4. Mass spectrometry-related data are available through the public depository MassIVE: MassIVE MSV000091640, [ftp://massive.ucsd.edu/MSV000091640/](http://massive.ucsd.edu/MSV000091640/).

The plasmid for the production of AAV1-VP3 (-M211V) is provided to academic research labs upon request via MTAs. Non-academic requestors are able to license the materials from the University of Florida.

#### SUPPLEMENTAL INFORMATION

Supplemental information can be found online at <https://doi.org/10.1016/j.omtm.2023.05.002>.

#### ACKNOWLEDGMENTS

We thank the UF-ICBR Electron Microscopy Core for the access to electron microscopes utilized for negative stain electron microscopy and cryo-EM screening. The TF20 cryo-electron microscope was provided by the UF College of Medicine (COM) and Division of

Sponsored Programs (DSP). Data collection at Florida State University was made possible by NIH grants S10 OD018142-01 Purchase of a direct electron camera for the Titan-Krios at FSU (PI Taylor) and S10 RR025080-01 Purchase of a FEI Titan Krios for 3-D EM (PI Taylor). The University of Florida COM, NIH GM082946 (PI R McKenna), provided partial funds for the research. Thermo Fisher Scientific provided funds for this study (AGR00021385 and AGR00023336).

## AUTHOR CONTRIBUTIONS

Conceptualization, M.M., R.M., and R.V.; investigation, M.M., W.L., K.M., A.B., A.N., K.G., P.C., X. F., X.F., and S.B.; writing – original draft, M.M. W.L., K.M., and R.V.; writing – review & editing, M.M., W.L., K.M., A.B., S.B., R.M., and R.V.; supervision, M.M., R.M., and R.V. All authors read and approved the final manuscript.

## DECLARATION OF INTERESTS

W.L., K.M., S.B., and R.V. are employees of Thermo Fisher Scientific.

## REFERENCES

- Rittié, L., Athanasopoulos, T., Calero-Garcia, M., Davies, M.L., Dow, D.J., Howe, S.J., Morrison, A., Ricciardelli, I., Saudemont, A., Jespers, L., and Clay, T.M. (2019). The landscape of early clinical gene therapies outside of oncology. *Mol. Ther.* 27, 1706–1717. <https://doi.org/10.1016/j.ymthe.2019.09.002>.
- Keeler, A.M., and Flotte, T.R. (2019). Recombinant adeno-associated virus gene therapy in light of Luxturna (and Zolgensma and Glybera): where are we, and how did we get here? *Annu. Rev. Virol.* 6, 601–621. <https://doi.org/10.1146/annurev-virology-092818-015530>.
- Schwartz, M., Likhite, S., and Meyer, K. (2021). Onasemnogene abeparvovec-xioi: a gene replacement strategy for the treatment of infants diagnosed with spinal muscular atrophy. *Drugs Today* 57, 387–399. <https://doi.org/10.1358/dot.2021.57.6.3264117>.
- Deng, C., Zhao, P.Y., Branham, K., Schlegel, D., Fahim, A.T., Jayasundera, T.K., Khan, N., and Besirli, C.G. (2022). Real-world outcomes of voretigene neparvovec treatment in pediatric patients with RPE65-associated Leber congenital amaurosis. *Graefes' archive for clinical and experimental ophthalmology = Albrecht von Graefes Archiv fur klinische und experimentelle Ophthalmologie*. <https://doi.org/10.1007/s00417-021-05508-2>.
- Keam, S.J. (2022). Eladocagene exuparvovec: first approval. *Drugs* 82, 1427–1432. <https://doi.org/10.1007/s40265-022-01775-3>.
- Blair, H.A. (2022). Valoctocogene roxaparvovec: first approval. *Drugs*. <https://doi.org/10.1007/s40265-022-01788-y>.
- Corti, M., Liberati, C., Smith, B.K., Lawson, L.A., Tuna, I.S., Conlon, T.J., Coleman, K.E., Islam, S., Herzog, R.W., Fuller, D.D., et al. (2017). Safety of intradiaphragmatic delivery of adeno-associated virus-mediated alpha-glucosidase (rAAV1-CMV-hGAA) gene therapy in children affected by pompe disease. *Hum. Gene Ther. Clin. Dev.* 28, 208–218. <https://doi.org/10.1089/humc.2017.146>.
- Mendell, J.R., Al-Zaidy, S.A., Rodino-Klapac, L.R., Goodspeed, K., Gray, S.J., Kay, C.N., Boye, S.L., Boye, S.E., George, L.A., Salabarria, S., et al. (2021). Current clinical applications of in vivo gene therapy with AAVs. *Mol. Ther.* 29, 464–488. <https://doi.org/10.1016/j.ymthe.2020.12.007>.
- Bowles, D.E., McPhee, S.W.J., Li, C., Gray, S.J., Samulski, J.J., Camp, A.S., Li, J., Wang, B., Monahan, P.E., Rabinowitz, J.E., et al. (2012). Phase 1 gene therapy for Duchenne muscular dystrophy using a translational optimized AAV vector. *Mol. Ther.* 20, 443–455. <https://doi.org/10.1038/mt.2011.237>.
- Bennett, A., Mietzsch, M., and Agbandje-McKenna, M. (2017). Understanding capsid assembly and genome packaging for adeno-associated viruses. *Future Virol.* 12, 283–297. <https://doi.org/10.2217/fvl-2017-0011>.
- Snijder, J., van de Waterbeemd, M., Damoc, E., Denisov, E., Grinfeld, D., Bennett, A., Agbandje-McKenna, M., Makarov, A., and Heck, A.J.R. (2014). Defining the stoichiometry and cargo load of viral and bacterial nanoparticles by Orbitrap mass spectrometry. *J. Am. Chem. Soc.* 136, 7295–7299. <https://doi.org/10.1021/ja502616y>.
- Wörner, T.P., Bennett, A., Habka, S., Snijder, J., Friese, O., Powers, T., Agbandje-McKenna, M., and Heck, A.J.R. (2021). Adeno-associated virus capsid assembly is divergent and stochastic. *Nat. Commun.* 12, 1642. <https://doi.org/10.1038/s41467-021-21935-5>.
- Kronenberg, S., Böttcher, B., von der Lieth, C.W., Bleker, S., and Kleinschmidt, J.A. (2005). A conformational change in the adeno-associated virus type 2 capsid leads to the exposure of hidden VP1 N termini. *J. Virol.* 79, 5296–5303. <https://doi.org/10.1128/JVI.79.9.5296-5303.2005>.
- Popa-Wagner, R., Porwal, M., Kann, M., Reuss, M., Weimer, M., Florin, L., and Kleinschmidt, J.A. (2012). Impact of VP1-specific protein sequence motifs on adeno-associated virus type 2 intracellular trafficking and nuclear entry. *J. Virol.* 86, 9163–9174. <https://doi.org/10.1128/JVI.00282-12>.
- Popa-Wagner, R., Sonntag, F., Schmidt, K., King, J., and Kleinschmidt, J.A. (2012). Nuclear translocation of adeno-associated virus type 2 capsid proteins for virion assembly. *J. Gen. Virol.* 93, 1887–1898. <https://doi.org/10.1099/vir.0.043232-0>.
- Sonntag, F., Schmidt, K., and Kleinschmidt, J.A. (2010). A viral assembly factor promotes AAV2 capsid formation in the nucleolus. *Proc. Natl. Acad. Sci. USA* 107, 10220–10225. <https://doi.org/10.1073/pnas.1001673107>.
- Mietzsch, M., Jose, A., Chipman, P., Bhattacharya, N., Daneshparvar, N., McKenna, R., and Agbandje-McKenna, M. (2021). Completion of the AAV structural atlas: serotype capsid structures reveals clade-specific features. *Viruses* 13. <https://doi.org/10.3390/v13010101>.
- Gao, G., Vandenberghe, L.H., Alvira, M.R., Lu, Y., Calcedo, R., Zhou, X., and Wilson, J.M. (2004). Clades of Adeno-associated viruses are widely disseminated in human tissues. *J. Virol.* 78, 6381–6388.
- Mietzsch, M., Penzes, J.J., and Agbandje-McKenna, M. (2019). Twenty-five years of structural parvirology. *Viruses* 11. <https://doi.org/10.3390/v11040362>.
- Stagg, S.M., Yoshioka, C., Davulcu, O., and Chapman, M.S. (2022). Cryo-electron microscopy of adeno-associated virus. *Chem. Rev.* 122, 14018–14054. <https://doi.org/10.1021/acs.chemrev.1c00936>.
- Joshi, P.R.H., Venereo-Sanchez, A., Chahal, P.S., and Kamen, A.A. (2021). Advancements in molecular design and bioprocessing of recombinant adeno-associated virus gene delivery vectors using the insect-cell baculovirus expression platform. *Biotechnol. J.* 16, e2000021. <https://doi.org/10.1002/biot.202000021>.
- Tan, E., Chin, C.S.H., Lim, Z.F.S., and Ng, S.K. (2021). HEK293 cell line as a platform to produce recombinant proteins and viral vectors. *Front. Bioeng. Biotechnol.* 9, 796991. <https://doi.org/10.3389/fbioe.2021.796991>.
- Mietzsch, M., Eddington, C., Jose, A., Hsi, J., Chipman, P., Henley, T., Choudhry, M., McKenna, R., and Agbandje-McKenna, M. (2021). Improved genome packaging efficiency of adeno-associated virus vectors using rep hybrids. *J. Virol.* 95, e0077321. <https://doi.org/10.1128/JVI.00773-21>.
- Rumachik, N.G., Malaker, S.A., Poweleit, N., Maynard, L.H., Adams, C.M., Leib, R.D., Cirolia, G., Thomas, D., Stamnes, S., Holt, K., et al. (2020). Methods matter: standard production platforms for recombinant AAV produce chemically and functionally distinct vectors. *Mol. Ther. Methods Clin. Dev.* 18, 98–118. <https://doi.org/10.1016/j.omtm.2020.05.018>.
- Burnham, B., Nass, S., Kong, E., Mattingly, M., Woodcock, D., Song, A., Wadsworth, S., Cheng, S.H., Scaria, A., and O'Riordan, C.R. (2015). Analytical ultracentrifugation as an approach to characterize recombinant adeno-associated viral vectors. *Hum. Gene Ther. Methods* 26, 228–242. <https://doi.org/10.1089/hgtb.2015.048>.
- Nass, S.A., Mattingly, M.A., Woodcock, D.A., Burnham, B.L., Ardinger, J.A., Osmond, S.E., Frederick, A.M., Scaria, A., Cheng, S.H., and O'Riordan, C.R. (2018). Universal method for the purification of recombinant AAV vectors of differing serotypes. *Mol. Ther. Methods Clin. Dev.* 9, 33–46. <https://doi.org/10.1016/j.omtm.2017.12.004>.
- Wagner, C., Innthaler, B., Lemmerer, M., Pletzenauer, R., and Birner-Gruenberger, R. (2022). Biophysical characterization of adeno-associated virus vectors using ion-exchange chromatography coupled to light scattering detectors. *Int. J. Mol. Sci.* 23, 12715. <https://doi.org/10.3390/ijms232112715>.
- Ebberink, E.H.T.M., Ruisinger, A., Nuebel, M., Thomann, M., and Heck, A.J.R. (2022). Assessing production variability in empty and filled adeno-associated viruses

- by single molecule mass analyses. *Mol. Ther. Methods Clin. Dev.* 27, 491–501. <https://doi.org/10.1016/j.omtm.2022.11.003>.
29. Strasser, L., Morgan, T.E., Guapo, F., Füssl, F., Forsey, D., Anderson, I., and Bones, J. (2021). A native mass spectrometry-based assay for rapid assessment of the empty:full capsid ratio in adeno-associated virus gene therapy products. *Anal. Chem.* 93, 12817–12821. <https://doi.org/10.1021/acs.analchem.1c02828>.
  30. Jin, X., Liu, L., Nass, S., O’Riordan, C., Pastor, E., and Zhang, X.K. (2017). Direct liquid chromatography/mass spectrometry analysis for complete characterization of recombinant adeno-associated virus capsid proteins. *Hum. Gene Ther. Methods* 28, 255–267. <https://doi.org/10.1089/hgtb.2016.178>.
  31. Harper, C.C., Miller, Z.M., Lee, H., Bischoff, A.J., Francis, M.B., Schaffer, D.V., and Williams, E.R. (2022). Effects of molecular size on resolution in charge detection mass spectrometry. *Anal. Chem.* 94, 11703–11712. <https://doi.org/10.1021/acs.analchem.2c02572>.
  32. Pierson, E.E., Keifer, D.Z., Asokan, A., and Jarrold, M.F. (2016). Resolving adeno-associated viral particle diversity with charge detection mass spectrometry. *Anal. Chem.* 88, 6718–6725. <https://doi.org/10.1021/acs.analchem.6b00883>.
  33. Barnes, L.F., Draper, B.E., Chen, Y.T., Powers, T.W., and Jarrold, M.F. (2021). Quantitative analysis of genome packaging in recombinant AAV vectors by charge detection mass spectrometry. *Mol. Ther. Methods Clin. Dev.* 23, 87–97. <https://doi.org/10.1016/j.omtm.2021.08.002>.
  34. Barnes, L.F., Draper, B.E., and Jarrold, M.F. (2022). Analysis of thermally driven structural changes, genome release, disassembly, and aggregation of recombinant AAV by CDMS. *Mol. Ther. Methods Clin. Dev.* 27, 327–336. <https://doi.org/10.1016/j.omtm.2022.10.008>.
  35. Werle, A.K., Powers, T.W., Zobel, J.F., Wappelhorst, C.N., Jarrold, M.F., Lykтей, N.A., Sloan, C.D.K., Wolf, A.J., Adams-Hall, S., Baldus, P., and Runnels, H.A. (2021). Comparison of analytical techniques to quantitate the capsid content of adeno-associated viral vectors. *Mol. Ther. Methods Clin. Dev.* 23, 254–262. <https://doi.org/10.1016/j.omtm.2021.08.009>.
  36. Wu, D., Hwang, P., Li, T., and Piszczek, G. (2022). Rapid characterization of adeno-associated virus (AAV) gene therapy vectors by mass photometry. *Gene Ther.* 29, 691–697. <https://doi.org/10.1038/s41434-021-00311-4>.
  37. Takeda, K., Noda, M., Maruno, T., and Uchiyama, S. (2023). Critical calibration of mass photometry for higher-mass samples such as adeno-associated virus vectors. *J. Pharm. Sci.* 112, 1145–1150. <https://doi.org/10.1016/j.xphs.2022.10.025>.
  38. McIntosh, N.L., Berguig, G.Y., Karim, O.A., Cortesio, C.L., De Angelis, R., Khan, A.A., Gold, D., Maga, J.A., and Bhat, V.S. (2021). Comprehensive characterization and quantification of adeno associated vectors by size exclusion chromatography and multi angle light scattering. *Sci. Rep.* 11, 3012. <https://doi.org/10.1038/s41598-021-82599-1>.
  39. Zolotukhin, S., Potter, M., Zolotukhin, I., Sakai, Y., Loiler, S., Fraitjes, T.J., Jr., Chiodo, V.A., Phillipsberg, T., Muzyczka, N., Hauswirth, W.W., et al. (2002). Production and purification of serotype 1, 2, and 5 recombinant adeno-associated viral vectors. *Methods* 28, 158–167.
  40. Potter, M., Lins, B., Mietzsch, M., Heilbronner, R., Van Vliet, K., Chipman, P., Agbandje-McKenna, M., Cleaver, B.D., Clément, N., Byrne, B.J., and Zolotukhin, S. (2014). A simplified purification protocol for recombinant adeno-associated virus vectors. *Mol. Ther. Methods Clin. Dev.* 1, 14034. <https://doi.org/10.1038/mtm.2014.34>.
  41. Dickerson, R., Argento, C., Pieracci, J., and Bakhshayeshi, M. (2021). Separating empty and full recombinant adeno-associated virus particles using isocratic anion exchange chromatography. *Biotechnol. J.* 16, e2000015. <https://doi.org/10.1002/biot.202000015>.
  42. Tamara, S., den Boer, M.A., and Heck, A.J.R. (2022). High-resolution native mass spectrometry. *Chem. Rev.* 122, 7269–7326. <https://doi.org/10.1021/acs.chemrev.1c00212>.
  43. Lantz, C., Wei, B., Zhao, B., Jung, W., Goring, A.K., Le, J., Miller, J., Loo, R.R.O., and Loo, J.A. (2022). Native top-down mass spectrometry with collisionally activated dissociation yields higher-order structure information for protein complexes. *J. Am. Chem. Soc.* 144, 21826–21830. <https://doi.org/10.1021/jacs.2c06726>.
  44. Fuerstenau, S.D., and Benner, W.H. (1995). Molecular weight determination of megadalton DNA electrospray ions using charge detection time-of-flight mass spectrometry. *Rapid Commun. Mass Spectrom.* 9, 1528–1538. <https://doi.org/10.1002/rcm.1290091513>.
  45. Fuerstenau, S.D., Benner, W.H., Thomas, J.J., Brugidou, C., Bothner, B., and Siuzdak, G. (2001). Mass spectrometry of an intact virus. *Angew. Chem.* 40, 541–544. [https://doi.org/10.1002/1521-3773\(20010202\)40:3<541::aid-anie541>3.0.co;2-k](https://doi.org/10.1002/1521-3773(20010202)40:3<541::aid-anie541>3.0.co;2-k).
  46. Elliott, A.G., Harper, C.C., Lin, H.W., Susa, A.C., Xia, Z., and Williams, E.R. (2017). Simultaneous measurements of mass and collisional cross-section of single ions with charge detection mass spectrometry. *Anal. Chem.* 89, 7701–7708. <https://doi.org/10.1021/acs.analchem.7b01675>.
  47. Elliott, A.G., Harper, C.C., Lin, H.W., and Williams, E.R. (2017). Mass, mobility and MS(n) measurements of single ions using charge detection mass spectrometry. *Analyst* 142, 2760–2769. <https://doi.org/10.1039/c7an00618g>.
  48. Harper, C.C., Elliott, A.G., Oltrogge, L.M., Savage, D.F., and Williams, E.R. (2019). Multiplexed charge detection mass spectrometry for high-throughput single ion analysis of large molecules. *Anal. Chem.* 91, 7458–7465. <https://doi.org/10.1021/acs.analchem.9b01669>.
  49. Contino, N.C., Pierson, E.E., Keifer, D.Z., and Jarrold, M.F. (2013). Charge detection mass spectrometry with resolved charge states. *J. Am. Soc. Mass Spectrom.* 24, 101–108. <https://doi.org/10.1007/s13361-012-0252-5>.
  50. Keifer, D.Z., Shinholt, D.L., and Jarrold, M.F. (2015). Charge detection mass spectrometry with almost perfect charge accuracy. *Anal. Chem.* 87, 10330–10337. <https://doi.org/10.1021/acs.analchem.5b02324>.
  51. O’Connor, D.M., Lutomski, C., Jarrold, M.F., Boulis, N.M., and Donsante, A. (2019). Lot-to-lot variation in adeno-associated virus serotype 9 (AAV9) preparations. *Hum. Gene Ther. Methods* 30, 214–225. <https://doi.org/10.1089/hgtb.2019.105>.
  52. Wörner, T.P., Snijder, J., Bennett, A., Agbandje-McKenna, M., Makarov, A.A., and Heck, A.J.R. (2020). Resolving heterogeneous macromolecular assemblies by Orbitrap-based single-particle charge detection mass spectrometry. *Nat. Methods* 17, 395–398. <https://doi.org/10.1038/s41592-020-0770-7>.
  53. Wörner, T.P., Aizikov, K., Snijder, J., Fort, K.L., Makarov, A.A., and Heck, A.J.R. (2022). Frequency chasing of individual megadalton ions in an Orbitrap analyser improves precision of analysis in single-molecule mass spectrometry. *Nat. Chem.* 14, 515–522. <https://doi.org/10.1038/s41557-022-00897-1>.
  54. Wörner, T.P., Snijder, J., Friese, O., Powers, T., and Heck, A.J.R. (2022). Assessment of genome packaging in AAVs using Orbitrap-based charge-detection mass spectrometry. *Mol. Ther. Methods Clin. Dev.* 24, 40–47. <https://doi.org/10.1016/j.omtm.2021.11.013>.
  55. Kostelic, M.M., Ryan, J.P., Brown, L.S., Jackson, T.W., Hsieh, C.C., Zak, C.K., Sanders, H.M., Liu, Y., Chen, V.S., Byrne, M., et al. (2022). Stability and dissociation of adeno-associated viral capsids by variable temperature-charge detection-mass spectrometry. *Anal. Chem.* 94, 11723–11727. <https://doi.org/10.1021/acs.analchem.2c02378>.
  56. Kafader, J.O., Beu, S.C., Early, B.P., Melani, R.D., Durbin, K.R., Zabrouskov, V., Makarov, A.A., Maze, J.T., Shinholt, D.L., Yip, P.F., et al. (2019). STORI plots enable accurate tracking of individual ion signals. *J. Am. Soc. Mass Spectrom.* 30, 2200–2203. <https://doi.org/10.1007/s13361-019-02309-0>.
  57. Kafader, J.O., Melani, R.D., Durbin, K.R., Ikwuagwu, B., Early, B.P., Fellers, R.T., Beu, S.C., Zabrouskov, V., Makarov, A.A., Maze, J.T., et al. (2020). Multiplexed mass spectrometry of individual ions improves measurement of proteoforms and their complexes. *Nat. Methods* 17, 391–394. <https://doi.org/10.1038/s41592-020-0764-5>.
  58. Mary, B., Maurya, S., Arumugam, S., Kumar, V., and Jayandharan, G.R. (2019). Post-translational modifications in capsid proteins of recombinant adeno-associated virus (AAV) 1-rh10 serotypes. *FEBS J.* 286, 4964–4981. <https://doi.org/10.1111/febs.15013>.
  59. Oyama, H., Ishii, K., Maruno, T., Torisu, T., and Uchiyama, S. (2021). Characterization of adeno-associated virus capsid proteins with two types of VP3-related components by capillary gel electrophoresis and mass spectrometry. *Hum. Gene Ther.* 32, 1403–1416. <https://doi.org/10.1089/hum.2021.009>.
  60. Liu, A.P., Patel, S.K., Xing, T., Yan, Y., Wang, S., and Li, N. (2020). Characterization of adeno-associated virus capsid proteins using hydrophilic interaction chromatography coupled with mass spectrometry. *J. Pharm. Biomed. Anal.* 189, 113481. <https://doi.org/10.1016/j.jpba.2020.113481>.
  61. Giglione, C., Boularot, A., and Meinel, T. (2004). Protein N-terminal methionine excision. *Cell. Mol. Life Sci.* 61, 1455–1474. <https://doi.org/10.1007/s00018-004-3466-8>.

62. Polevoda, B., and Sherman, F. (2000). Nalpha-terminal acetylation of eukaryotic proteins. *J. Biol. Chem.* 275, 36479–36482. <https://doi.org/10.1074/jbc.R000023200>.
63. Gao, G.P., Alvira, M.R., Wang, L., Calcedo, R., Johnston, J., and Wilson, J.M. (2002). Novel adeno-associated viruses from rhesus monkeys as vectors for human gene therapy. *Proc. Natl. Acad. Sci. USA* 99, 11854–11859.
64. Mietzsch, M., Barnes, C., Hull, J.A., Chipman, P., Xie, J., Bhattacharya, N., Sousa, D., McKenna, R., Gao, G., and Agbandje-McKenna, M. (2020). Comparative analysis of the capsid structures of AAVrh.10, AAVrh.39, and AAV8. *J. Virol.* 94, 017699–e1819. <https://doi.org/10.1128/JVI.01769-19>.
65. Mietzsch, M., Li, Y., Kurian, J., Smith, J.K., Chipman, P., McKenna, R., Yang, L., and Agbandje-McKenna, M. (2020). Structural characterization of a bat Adeno-associated virus capsid. *J. Struct. Biol.* 211, 107547. <https://doi.org/10.1016/j.jsb.2020.107547>.
66. Halder, S., Van Vliet, K., Smith, J.K., Duong, T.T.P., McKenna, R., Wilson, J.M., and Agbandje-McKenna, M. (2015). Structure of neurotropic adeno-associated virus AAVrh.8. *J. Struct. Biol.* 192, 21–36. <https://doi.org/10.1016/j.jsb.2015.08.017>.
67. Zolotukhin, S., Byrne, B.J., Mason, E., Zolotukhin, I., Potter, M., Chesnut, K., Summerford, C., Samulski, R.J., and Muzyczka, N. (1999). Recombinant adeno-associated virus purification using novel methods improves infectious titer and yield. *Gene Ther.* 6, 973–985.
68. Mietzsch, M., Smith, J.K., Yu, J.C., Banala, V., Emmanuel, S.N., Jose, A., Chipman, P., Bhattacharya, N., McKenna, R., and Agbandje-McKenna, M. (2020). Characterization of AAV-specific affinity ligands: consequences for vector purification and development strategies. *Mol. Ther. Methods Clin. Dev.* 19, 362–373. <https://doi.org/10.1016/j.omtm.2020.10.001>.
69. Zheng, S.Q., Palovcak, E., Armache, J.P., Verba, K.A., Cheng, Y., and Agard, D.A. (2017). MotionCor2: anisotropic correction of beam-induced motion for improved cryo-electron microscopy. *Nat. Methods* 14, 331–332. <https://doi.org/10.1038/nmeth.4193>.
70. Grant, T., Rohou, A., and Grigorieff, N. (2018). cisTEM, user-friendly software for single-particle image processing. *Elife* 7, e35383. <https://doi.org/10.7554/eLife.35383>.
71. Pettersen, E.F., Goddard, T.D., Huang, C.C., Couch, G.S., Greenblatt, D.M., Meng, E.C., and Ferrin, T.E. (2004). UCSF Chimera—a visualization system for exploratory research and analysis. *J. Comput. Chem.* 25, 1605–1612. <https://doi.org/10.1002/jcc.20084>.
72. Emsley, P., and Cowtan, K. (2004). Coot: model-building tools for molecular graphics. *Acta Crystallogr. D Biol. Crystallogr.* 60, 2126–2132. <https://doi.org/10.1107/s0907444904019158>.
73. Adams, P.D., Afonine, P.V., Bunkóczi, G., Chen, V.B., Davis, I.W., Echols, N., Headd, J.J., Hung, L.W., Kapral, G.J., Grosse-Kunstleve, R.W., et al. (2010). PHENIX: a comprehensive Python-based system for macromolecular structure solution. *Acta Crystallogr. D Biol. Crystallogr.* 66, 213–221. <https://doi.org/10.1107/s0907444909052925>.